The Astrophysical Journal, 882:7 (12pp), 2019 September 1 https://doi.org/10.3847/1538-4357/ab304f

Impulsive Coronal Heating from Large-scale Magnetic Rearrangements: From IRIS to *SDO*/AIA

Fabio Reale[1,2], Paola Testa[3], Antonino Petralia[2], and David R. Graham[4]
[1] Dipartimento di Fisica & Chimica, Università di Palermo, Piazza del Parlamento 1, I-90134 Palermo, Italy; fabio.reale@unipa.it
[2] INAF-Osservatorio Astronomico di Palermo, Piazza del Parlamento 1, I-90134 Palermo, Italy
[3] Center for Astrophysics | Harvard & Smithsonian, 60 Garden Street, Cambridge, MA 02138, USA
[4] Bay Area Environmental Research Institute, NASA Research Park, Moffett Field, CA, CA 94952, USA
Received 2019 April 15; revised 2019 July 3; accepted 2019 July 3; published 2019 August 26

Abstract

The Interface Region Imaging Spectrograph (IRIS) has observed bright spots at the transition region footpoints associated with heating in the overlying loops, as observed by coronal imagers. Some of these brightenings show significant blueshifts in the Si IV line at 1402.77 Å ($\log T\,[\mathrm{K}] \approx 4.9$). Such blueshifts cannot be reproduced by coronal loop models assuming heating by thermal conduction only, but are consistent with electron beam heating, highlighting for the first time the possible importance of nonthermal electrons in the heating of nonflaring active regions. Here we report on the coronal counterparts of these brightenings observed in the hot channels of the Atmospheric Imaging Assembly on board the *Solar Dynamics Observatory*. We show that the IRIS bright spots are the footpoints of very hot and transient coronal loops that clearly experience strong magnetic interactions and rearrangements, thus confirming the impulsive nature of the heating and providing important constraints for their physical interpretation.

Key words: Sun: activity – Sun: corona – Sun: UV radiation

Supporting material: animations

1. Introduction

Impulsive events play a major role in the corona. Flares are the most prominent, but they are believed to scale down to a population of smaller events (nanoflares) (e.g., Hudson 1991; Argiroffi et al. 2008; Aschwanden et al. 2008; Hannah et al. 2011).

One key question concerns details of the properties and origin of the impulsive energy release. Signatures of the energy release itself are often obscured by the violent heating and ionization in the lower atmosphere, sometimes saturating detectors (e.g., Lin et al. 2001). Accurate, occasionally fortuitous, positioning of the instrument and fast sampling are essential to glimpse preimpulsive epoch signatures (see Jeffrey et al. 2018), although such observations are rare. At the other extreme, a diffuse nanoflaring activity is extremely elusive, because nanoflare storms driven by chaotic magnetic braiding (e.g., Parker 1988) leave faint and ambiguous signatures (e.g., Klimchuk 2006).

Events at intermediate scales are therefore fundamental to capture the basic mechanisms of impulsive energy releases in the solar corona. Events recently captured by the Interface Region Imaging Spectrograph (IRIS) observations are excellent candidates. As shown by Testa et al. (2014), IRIS detected significant Doppler shifts during the brightening of hot spots inside active regions observed in the transition region in the Si IV line at 1402.77 Å ($T \approx 10^{4.9}$ K). The brightenings are highly variable, with a typical duration of 20–60 s. Some of them show moderate blueshifts with typical velocities of $\sim$15 km s^{-1}. The blueshifts could not be reproduced by hydrodynamic models of plasma confined in a loop where the heat pulse is transported along the loop exclusively by thermal conduction. Instead, they were consistently reproduced by models where the heating is driven by beams of nonthermal electrons streaming down along the loop and hitting the dense plasma at the footpoints (Testa et al. 2014; Polito et al. 2018). The energy distribution of the electron beams is typically described with a power law, with a low-energy cutoff E_C. Comparison with the models shows that the observed blueshifted transition region brightenings can be reproduced by heating deposited on small timescales ($\leqslant$30 s), characterized by total energy of $\leqslant 10^{25}$ erg, and with low-energy cutoff $E_c \sim 10$ keV (Testa et al. 2014; Polito et al. 2018), lower than in major flares where larger energies are involved (e.g., Hannah et al. 2011). Although less energetic, the presence of such electron beams is a major indication of magnetic reconnection (Priest & Forbes 2000; Cargill et al. 2015).

The present study is devoted to a systematic study of the coronal counterparts of the brightenings observed with IRIS (P. Testa et al. 2019, in preparation). As mentioned above, Testa et al. (2014) have already shown that there is a clear correspondence between IRIS brightenings and the ignition of loop systems, in particular, visible in hot EUV channels of the Atmospheric Imaging Assembly (AIA) on board the *Solar Dynamics Observatory* (*SDO*). Here we will focus on this correspondence and analyze the features of the loop systems.

Coronal loops outside of flares but at temperatures above 5–6 MK have been extensively observed and studied in the past. Most studies focused on demonstrating that these coronal loops were really the site of very hot plasma, with the detection of emission from single very hot lines (Ko et al. 2009; Testa & Reale 2012), of very hot components in broadband spectra (Miceli et al. 2012), hard X-rays (McTiernan 2009; Ishikawa et al. 2017; Marsh et al. 2018), and imaging from narrowband EUV (Reale et al. 2011; Brosius et al. 2014) and broadband X-rays (Porter & Klimchuk 1995; Reale et al. 2009). Also, emission measure reconstruction recovered small very hot components in active region loops (Petralia et al. 2014; Ishikawa et al. 2017; Parenti et al. 2017). These studies either analyzed active regions as a whole, or distinctly single loops.

Table 1
Transient EUV Events with Corresponding Hot Spots in IRIS Observations

N	Date	Time	X	Y
1	2014 Feb 4	13:34:49	399.7	−77.6
2	2014 Feb 23	23:24:37	169.4	−60.7
3	2014 Mar 19	15:15:25	71.2	303.6
4	2014 Apr 10	02:42:01	822.7	−134.3
5	2014 Sep 17	14:52:01	−138.1	91.8
6	2014 Sep 17	17:15:01	−99.1	74.1
7	2014 Sep 18	08:06:01	34.4	74.7
8	2015 Jan 29	18:29:01	149.8	−78.6
9	2015 Nov 12	01:37:12	−117.2	−329.6
10	2015 Dec 24	15:17:00	−597.7	−352.1

Note. The time (UT) is taken just before the beginning of the event, the one of the image for background subtraction (94 Å). The coordinates [X, Y] are of the center of the data set (arcsec).

In this study we will show that very hot loops corresponding to IRIS hot spots are to be treated as systems of interacting loops, and it is probably this interaction that determines the high temperature and the coherent behavior that make them intermediate between proper single flares and storms of nanoflares.

Section 2 describes the data, and the results are discussed in Section 3.

2. The Observations and Data Analysis

The AIA (Lemen et al. 2012) on board the *SDO* is based on normal-incidence optics and is equipped with six narrowband filters in the EUV band (94–335 Å) that contain a few strong spectral lines that sample the solar corona in a wide temperature range, approximately between 0.5 and 10 MK (Boerner et al. 2012, 2014). The instrument continuously monitors the full-disk corona with high cadence (12 s) and a pixel size of $\sim 0\farcs6$.

In this study we focus on the evolution of hot arch-like structures whose footpoints correspond to hot spots detected in the Si IV 1400 Å passband with IRIS. In particular, we analyze the evolution observed in the two AIA channels that are most sensitive to plasma at temperatures higher than 5 MK. The 94 Å and 131 Å channels include highly ionized Fe lines and Fe XVIII and Fe XXI lines, respectively, that are sensitive to plasma at temperatures in the ranges 6–8 MK, and 9–12 MK, respectively. We point out that both 94 and 131 Å channels also include other intense Fe lines (Fe IX, Fe X for 94 Å and Fe VIII for 131 Å; Foster & Testa 2011; Lemen et al. 2012) that generally dominate the sensitivity of these two passbands at the lower temperatures (0.5–1 MK; e.g., Martínez-Sykora et al. 2011), which we are not interested in here. It is worth noting though that the cool (transition region) contribution to these bands is quite limited in hot active region core loops studied here (e.g., Testa et al. 2012).

Based on IRIS evidence in the Si IV 1400 Å passband, we have selected 10 events that occurred between 2014 February and 2015 December, listed in Table 1. In all of them, we see brightenings in both hot AIA channels. All of them are below the threshold for flare detection in *Geostationary Operational Environmental Satellite* light curves.

We have ascertained that all of the events share a set of common features that we describe in the following. Furthermore, we show a more detailed analysis for three of them where the evolution is particularly clear and yield good counts; one of them we study in greater detail.

The relevant image sequences have been preprocessed with the standard AIA software procedure and coaligned. In order to study the evolution of the coronal structures in greater detail, we have devised procedures to highlight them above the underlying present emission. Our approach to this has been to subtract the emission just before the brightenings. This allows us to subtract the contribution from the plasma in the temperature range 0.5–1 MK and to study exclusively the transient brightening of the hotter plasma (>6 MK).

2.1. Loop Evolution

We focus our attention on the event on 2015 November 12 (Event 9 in Table 1) starting approximately at 1:38 UT. Figures 1–3 (and Figure 9 in Appendix A) show the loop system and its evolution. Figure 1 shows the loop region in the *SDO*/AIA 94 Å channel, the corresponding magnetogram, and the same region as imaged with IRIS in the Si IV 1400 Å passband. In panel (a) the image is obtained after integrating over 100 images around the event. The system consists of several arches that apparently intersect each other at large angles ($\gtrsim 20^{\circ}$) in the plane of the sky. Moss-like structures are widespread in the image, which are related to the cool-sensitive side of the double-peaked channel response function.

In panel (b) the magnetogram shows that the visible arches connect regions with opposite magnetic polarity. The IRIS observation shows the bright features at some loop footpoints. Figures 2(a)–(d) (and the left-hand side of Figure 9 in Appendix A) shows the evolution of the loop system as imaged in the 94 Å channel. The brightening clearly starts from the footpoints (Figure 2(a)). Then the brightening propagates along the loop legs. At least three different loops appear to brighten almost at the same time (Figure 2(b)). A couple of them appear to intersect along the line of sight ($X = 80''$, $Y = 60''$). Around 4 minutes after the first brightening, a whole complex loop system appears to be bright (Figure 2(c)): we distinguish several loops, a longer one that extends from left to right and is curved downward. The system then begins to fade (Figure 2(d)). The distance between the footpoints (see line A in Figure 2(e)) is approximately 57 Mm, which leads to a presumable upper limit for the total length of a semicircular loop of ∼90 Mm. Among the others loops, we see at least two of them crossing the major one, whose distances between the footpoints are named C and D in Figure 2(e), and are 32 Mm and 36 Mm, respectively (upper limit for length 50 Mm and 57 Mm, respectively). As shown in Figure 2(f), the arc-like structures make (apparent angles of 40° and 52°, respectively, in the plane of the sky.

Figure 3 shows three snapshots of the loop system taken in the 131 Å channel after background subtraction (see the right-hand side of Figure 9 in Appendix A for the evolution in this channel). In general, in this channel we see fewer bright loops at a time and the 131 Å emission is shorter lived, compared to the cooler 94 Å emission. In the earlier image, the two footpoints that brighten first are clearly visible. In the second image, we see a very similar topology as in the corresponding image in the 94 Å channel (Figure 2(b)). In the third one, we can distinguish the longest loop structure.

This evolution has a clear correspondence in the light curves integrated over the frames in Figures 2–3, i.e., over the whole loop system, in both channels, shown in Figure 4. In the 131 Å

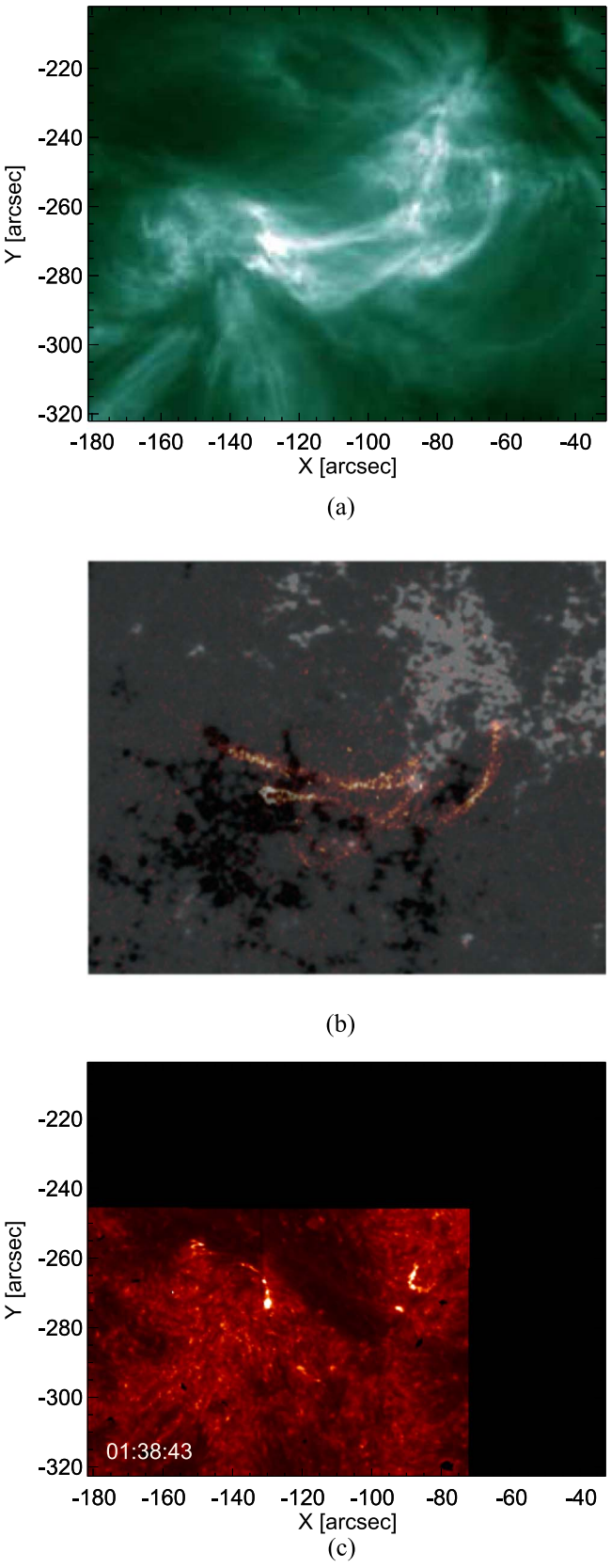

Figure 1. Loop system overlying short-lived UV transition region brightenings detected by IRIS, observed on 2015 November 12 (Event 9 in Table 1). (a) Field of view as observed in the AIA 94 Å channel after integrating 100 images (no background subtraction). (b) Magnetogram ($-100 < B < 100$ G, black and white) over the 94 Å image (red, panel (c) in Figure 2). (c) IRIS Si IV 1400 Å passband image at the labeled time. The coordinates are heliocentric.

channel, the emission has an early sharp peak (time $t \approx 400$ s), remains relatively steady for the next ~10 minutes, and then decays rapidly. In the 94 Å channel, the evolution is more gradual and delayed. The emission smoothly reaches its peak at $t \approx 650$ s, i.e., ~4 minutes later than in the other channel, and then continuously and gradually decreases.

A couple of other cases are shown in Figures 5 and 6 (Events 7 and 5 in Table 1, respectively, and Figures 10 and 11 in Appendix A). The loop system shown in Figure 5 is simpler than that in Figure 2 but similarly shows the presence of a misaligned loop bundle (Figure 5(a)). Entangled loops are visible in the 131 Å channel (Figure 5(b)). The overall evolution is faster and the light curves simpler too, but they share with the previous case the earlier 131 Å peak and the smoother curve in the 94 Å channel (Figure 5(e)). The footpoint distances marked in Figure 5(c) are 46 Mm (E) and 72 Mm (F) (upper limits for loop lengths 72 Mm and 113 Mm, respectively). A representative angle between misaligned structures is 22° as shown in Figure 5(d).

The loop system shown in Figure 6 is more complex than that in Figure 5. As is clear in the 94 Å channel (Figure 6(a)), there are both quasi-parallel, probably entangled, loops and other oblique but intersecting loops. The whole system appears as a more compact bundle than the other two. The core loops are also very bright in the 131 Å channel (Figure 6(b)). As representative sizes, we measure footpoint distances of 65 Mm (G) and 69 Mm (H) (Figure 6(c)) and a representative angle between the misaligned structure is 22° (Figure 6(d)). Also, in this case the rise and the peak in the light curve in the 131 Å channel are anticipated with respect to those in the 94 Å channel (Figure 6(e)). However, differing from the other cases, here we clearly see two different peaks in both channels, one ~5 minutes after the other, which most probably mark the presence of two distinct heating episodes.

2.2. Emission Measure Evolution

One key question of this analysis is whether the plasma that becomes transiently bright in the 94 and 131 Å channels is really very hot. Although the simultaneous brightening in the two channels after background subtraction and their timing is perfectly compatible with them heated to and cooling from temperatures above 10^7 K, we derive more constraints about the thermal composition of the brightening plasma from a reconstruction of the emission measure distribution along the line of sight. In particular, we select a few locations in the brightest areas of the first brightening region and we use all AIA channels for the reconstruction.

In order to derive information on the thermal evolution of the observed transient coronal loops, we apply an inversion method (Cheung et al. 2015) to the time series of the six coronal AIA passband (94, 131, 171, 193, 211, 335 Å) to obtain the differential emission measure (DEM). The inversion method considers the full response functions including hot and cool contributions in the double-peaked channels. Cheung et al. (2015) thoroughly discuss the validation of the method and the estimation of the associated uncertainties; they conclude that the method is overall accurate in recovering the general properties of the DEM and its evolution (though more detailed properties, such as, e.g., DEM slopes at the high temperature end might not be constrained too well).

We subtract as background an image for each passband taken before the events starts (2015-11-12T01:37:54). The

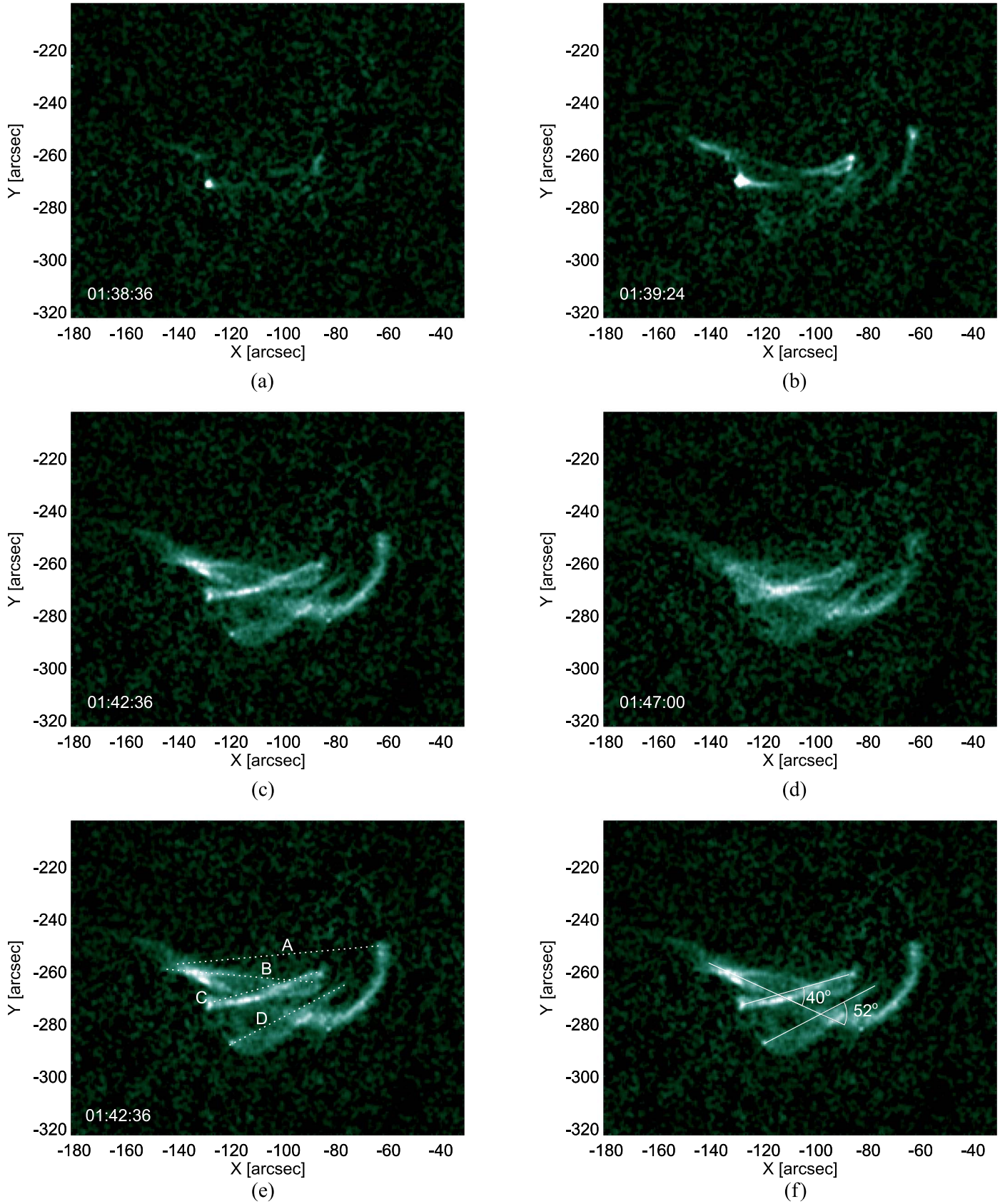

Figure 2. Loop system in Figure 1. ((a)–(d)) Evolution of the loop system in the 94 Å channel after subtracting an image just before the brightening begins (1:37:12 UT). The frame times are labeled (see the left-hand side of Figure 9 in Appendix A for an animation of this evolution); (e) relevant footpoint connections; (f) angles between intersecting arches.

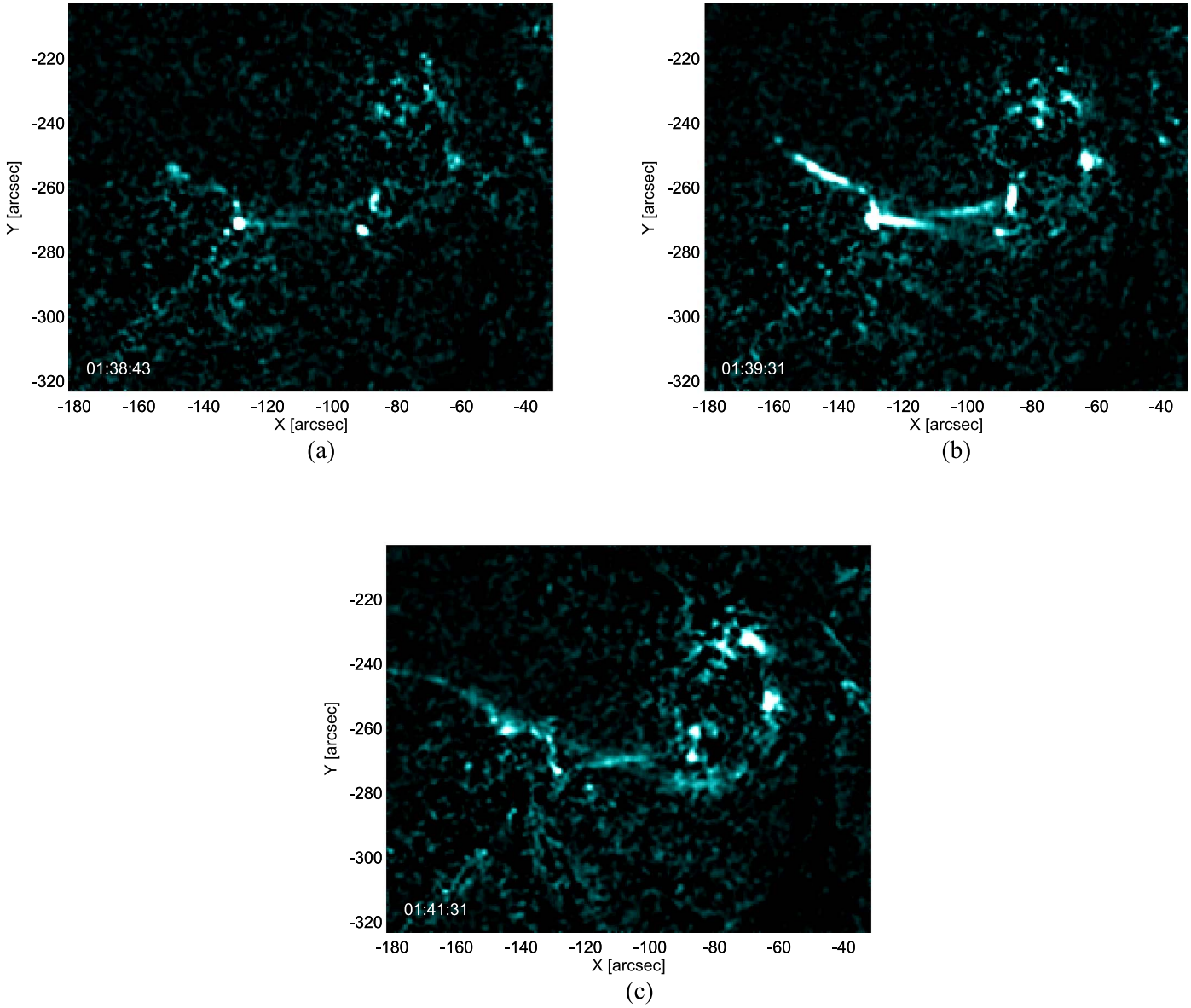

Figure 3. Three representative snapshots of the loop system of Figure 2 as observed in the AIA 131 Å channel (see the right-hand side of Figure 9 in Appendix A for the related animation).

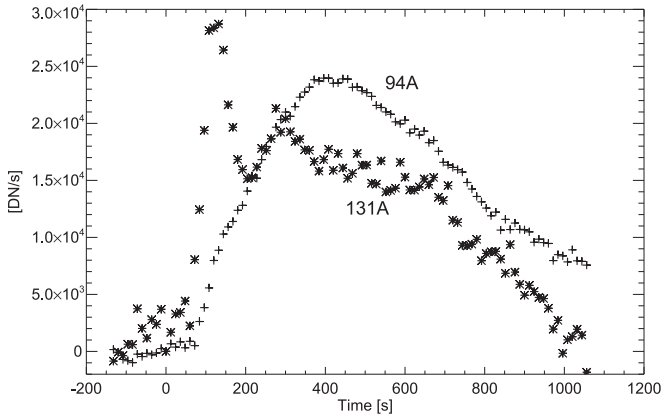

Figure 4. Light curves integrated over the frames in Figures 2 and 3 in the 94 Å (crosses) and 131 Å (stars) channels (seconds since 01:37:12 UT). The emission is background subtracted.

observed emission (I_i, in units of DN s^{-1} pix^{-1}) in each of these AIA narrowband EUV channels depends on the thermal properties of the optically thin coronal plasma in the pixel, as

$$I_i = \int_T R_i(T)\mathrm{DEM}(T)\, dT, \quad (1)$$

where $R_i(T)$ is the response function in a given passband (in units of DN cm^5 s^{-1} pix^{-1}), and the DEM (in units of cm^{-5} K^{-1}) is defined by $\mathrm{DEM}(T)\, dT = \int_z n_e^2(T)\, dz$, where $n_e^2(T)$ is the electron density of the plasma at temperature T. We will show plots (Figure 7) of the distribution of emission measure (EM; in units of cm^{-5}) as a function of temperature, which is obtained by integrating the DEM(T) over 0.2 log T [K] temperature ranges.

The light curves are taken in single pixels and are therefore noisier than those shown in Figure 4, but each of them equally shows a well-defined peak that is delayed in the 94 Å channel

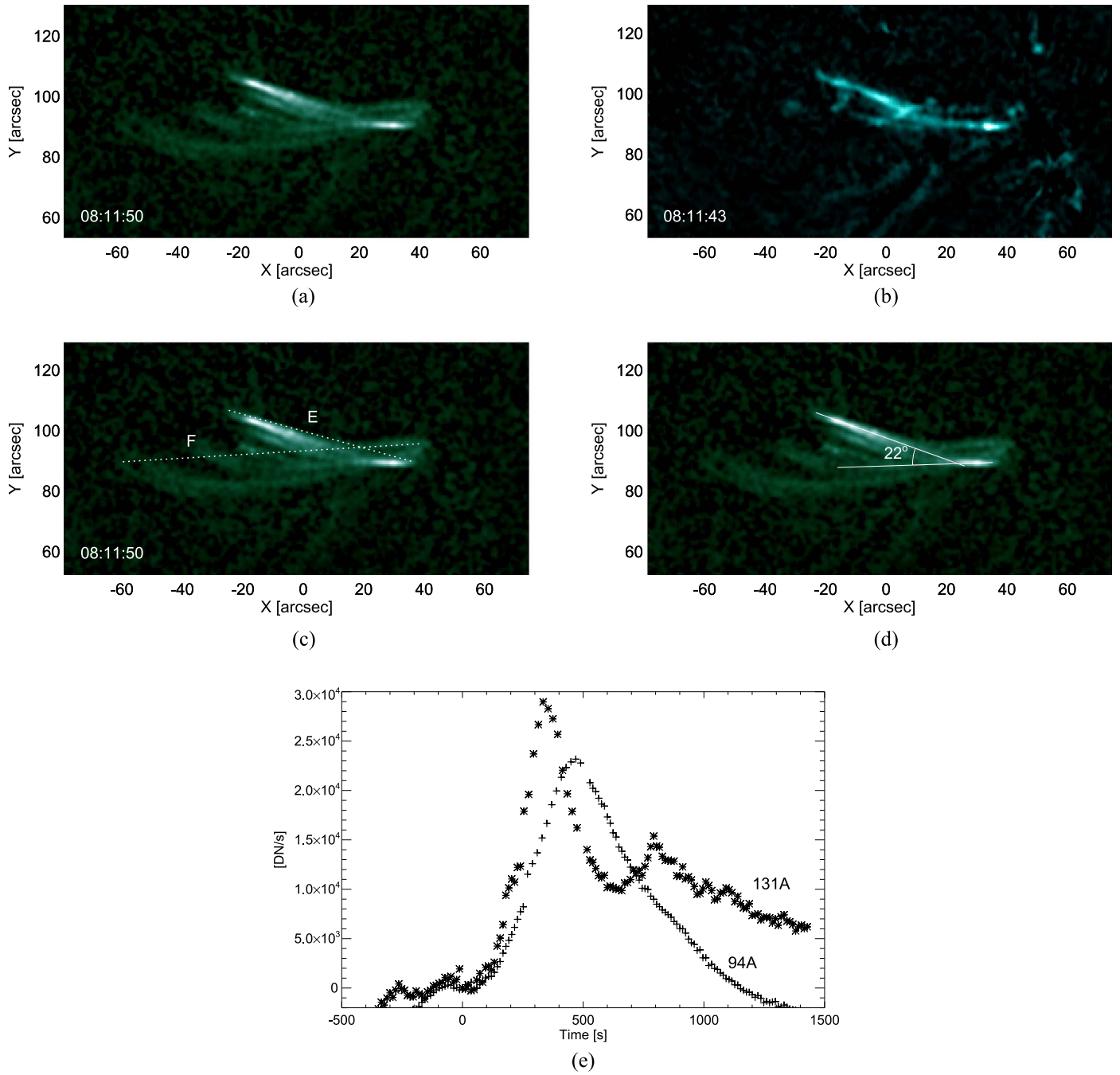

Figure 5. Loop system that corresponds to UV bright spots detected by IRIS, observed on 2014 September 18 (Event 7 in Table 1). Background-subtracted image of the loop system at its maximum brightness observed (a) in the AIA 94 Å channel and (b) in the 131 Å channel (see Figure 10 in Appendix A for the related animation); ((c), (d)) as Figures 2(e), (f); (e) light curves (seconds since 08:06:01 UT).

(Figure 4(b)). The peaks occur between 400 and 600 s and the delay of the 94 Å channel looks somewhat larger in points A1 and C1, possibly connected to the fact that they are at the intersection of different structures. The distributions in the right column of Figure 7 have clear peaks generally around $\log T\,[\mathrm{K}] \sim 6.8$. However, a very hot and significant component above 10^7 K is present, thus confirming the evidence from simple inspection of the images and from light curves. Also in this case, the evolution of the distributions in A1 and C1 is similar and looks different from that in B1 and C1. In A1 and C1 we see a smooth increasing and decreasing trend and the peak seems to be hotter when the emission measure is lower. In B1 and D1 the distributions are generally broader, do not shift in temperature, and their evolution is less smooth. The spatial and temporal coherence of the DEMs, and in particular of its hot components, also supports the reliability of the DEM results obtained with the method (see Figure 8).

3. Discussion

The systematic analysis of the coronal loops overlying the brightenings imaged by the IRIS mission, especially in the

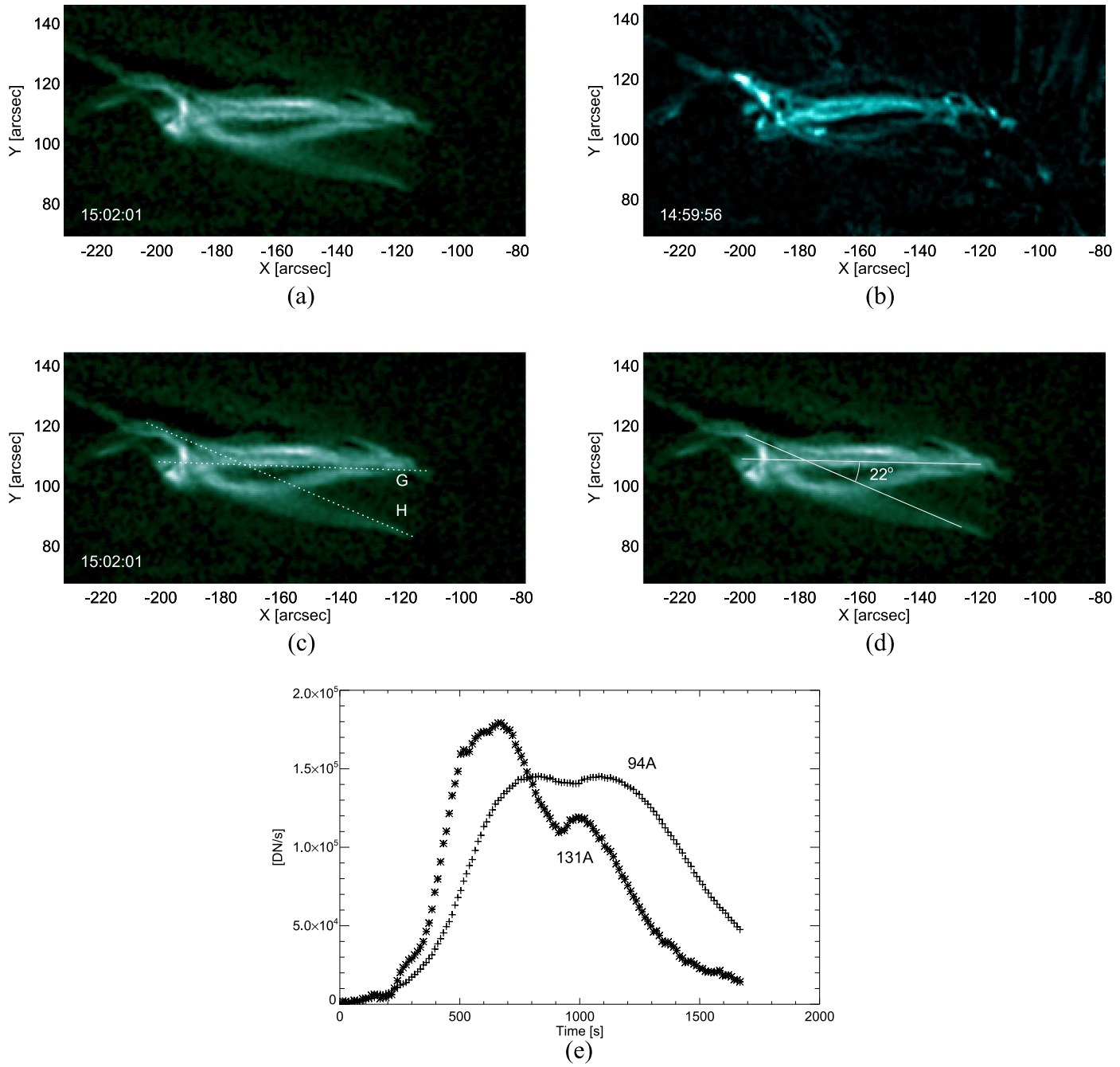

Figure 6. As in Figure 5 for the loop system that corresponds to UV bright spots detected by IRIS, observed on 2014 September 17 (Event 5 in Table 1, seconds since 14:52:01 UT; see Figure 11 in Appendix A for the related animation).

Si IV 1400 Å passband, shows that in all cases they correspond to the ignition of complex loop systems to high temperatures (8–10 MK) very bright in the hottest *SDO*/AIA EUV channels, namely, the 94 Å and the 131 Å channels.

One important implication of the observed evolution in the hot 94 and 131 Å AIA channels and of the emission measure analysis is that the involved plasma is heated above typical persistent active region temperatures, with detected peak temperatures typically up to 8–10 MK. We note that Mitra-Kraev & Del Zanna (2019) find a case of a microflare, in which the 94 Å emission can be explained by plasma at lower temperatures (∼5 MK), in contrast with these findings.

The timescales involved are longer than expected. The loop decay times can be estimated as

$$\tau_d \approx 15 \frac{L_{\rm Mm}}{\sqrt{T_7}} \ {\rm s}, \qquad (2)$$

where $L_{\rm Mm}$ is the loop half-length in units of Mm and T_7 is the loop maximum temperature in units of 10^7 K (Reale 2007). If we consider the case shown in Figures 2–4, for the maximum possible half-length (∼50 Mm) and for a maximum temperature of ∼10 MK (the dependence is relatively weak), we obtain $\tau_d \sim 800$ s. This might look in relative agreement with

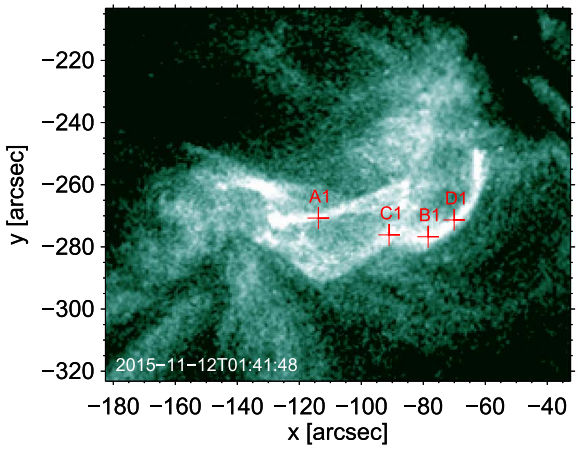

(a)

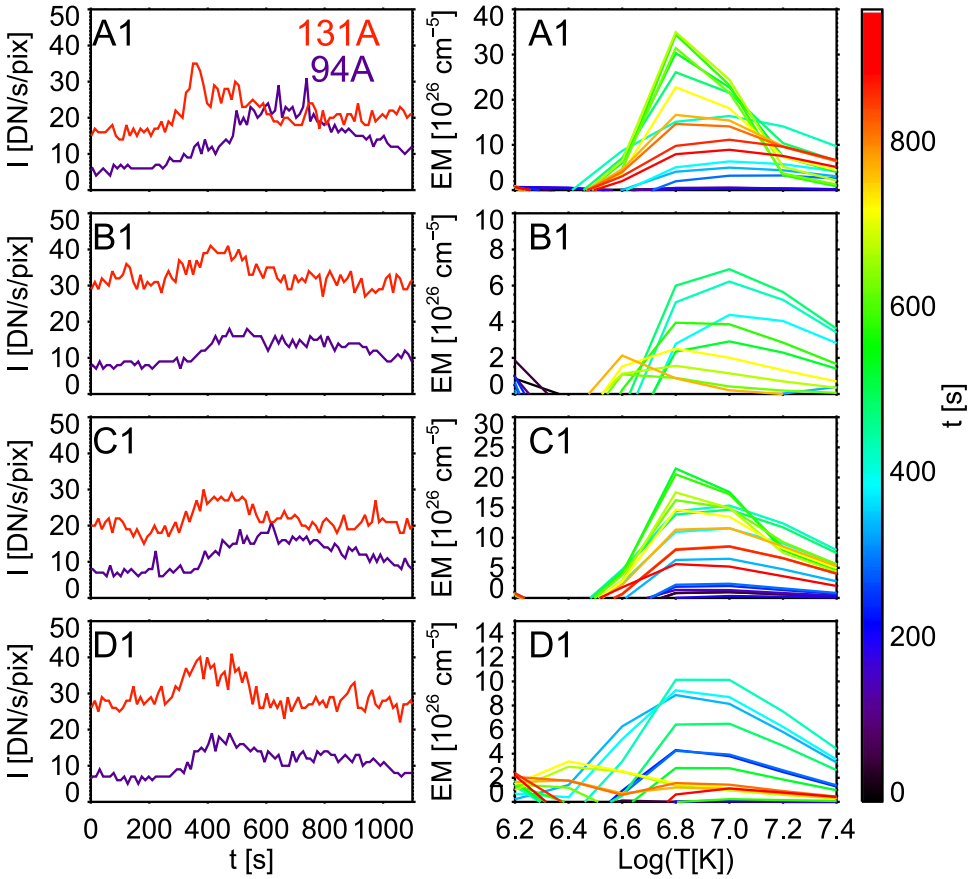

(b)

Figure 7. Light curves in the AIA 94 and 131 Å passbands ((b), left column) and evolution of emission measure distribution ((b), right column), for four locations (marked in panel (a)) in the hot transient coronal loops shown in Figures 1–4 (Event 9 in Table 1). The emission measure distributions vs. temperature are shown at progressive times from 0 (black) to 1000 (red) s. For both light curves and EM vs. T the reference time used is 01:33:54 UT.

the observed decay time in Figure 4, but we should consider that the channels are narrowband filters, with relatively narrow ranges of temperature sensitivity, typically much narrower than broadband X-ray filters (e.g., Narukage et al. 2011), and the emission should be observed for a much shorter time. As a rough estimate, assuming an exponential cooling, the time interval Δt in which the emission is observed in a given channel is

$$\Delta t \approx -\tau_d \ln\left(1 - \frac{\Delta T}{T_0}\right), \quad (3)$$

where ΔT is the temperature range that the channel is sensitive to and T_0 is the maximum temperature. Taking $\Delta T \sim 5$ MK (this

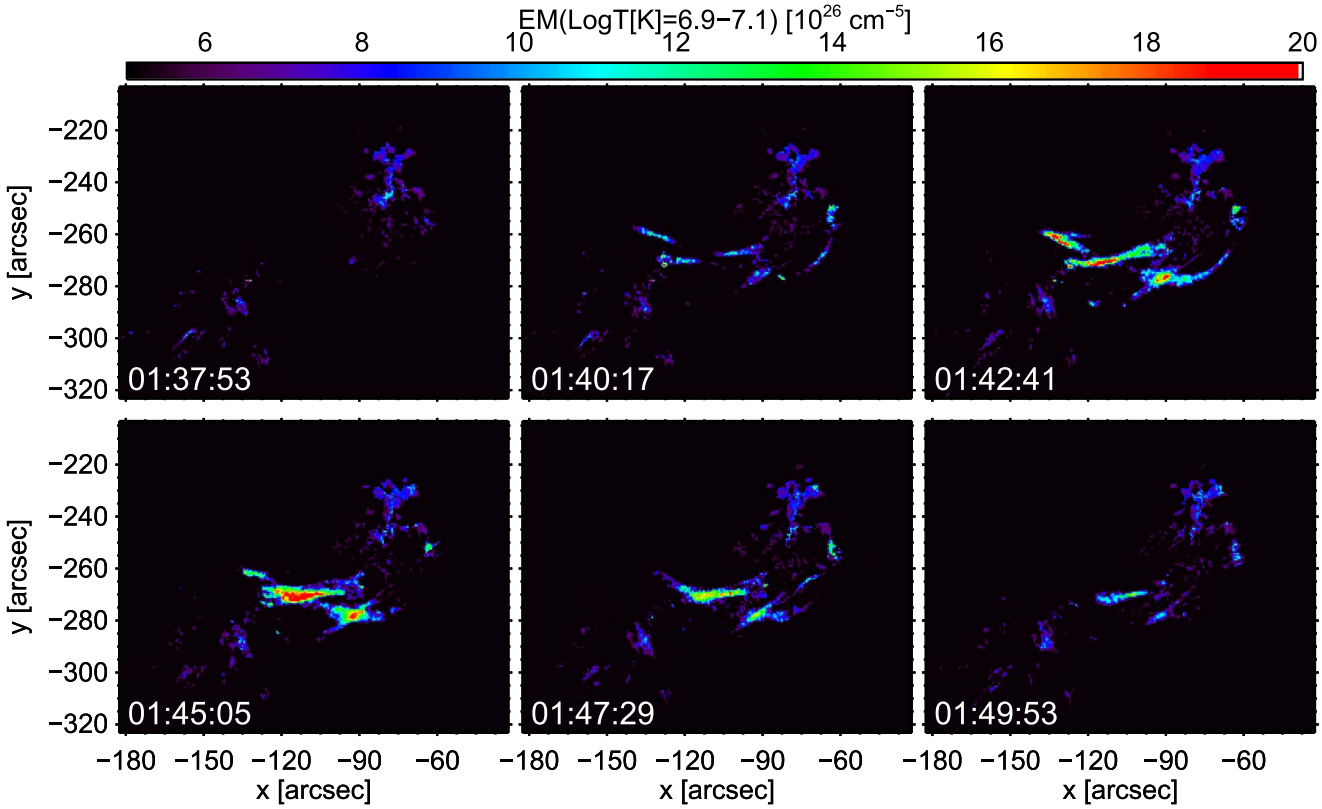

Figure 8. Maps of emission measure in the temperature bin $\log T\,[\mathrm{K}] = 6.9 - 7.1$ at the six labeled times for the same event as in Figure 7.

should hold for both channels) and $T_0 \sim 15$ MK as typical values, we obtain $\Delta t \sim 250$ s, much less than the time we observe emission in the hot channels. There are at least two good reasons why we observe the emission for longer than expected. One is that Equation (2) was derived for conditions of energy equilibrium (Serio et al. 1991). Energy equilibrium implies that the density is very high, to match the high maximum temperature. This is probably not the case here because the evolution suggests a short heat pulse that does not allow each loop to reach such high density. A lower density drives a slower radiative cooling. The second reason is that, as apparent from the observation itself, we are not capturing a single heating episode but most probably several of them, which determine the brightening of several loops. The light curve is therefore the envelope of unresolved brightenings, and we are more likely detecting the evolution of the total energy release in the loop system. The same kind of analysis can be applied to the other events, and it is even more evident for the third where we are clearly detecting two distinct heating episodes.

As a general overview, all the coronal loop heating events for which IRIS observes rapid footpoints brightenings in the transition region and chromosphere share common features, and in particular a complex magnetic configuration in the corona. We see in all cases misaligned magnetic arches that most likely interact with each other determining impulsive energy releases. We may simply address them as large-scale magnetic rearrangements, probably driven by large-scale photospheric motions or large-scale magnetic flux emergence. The interaction of misaligned magnetic channels determines large-scale magnetic reconnection, which in turn leads to an impulsive energy release coherent in space and time across the structures. Independent signatures of this are the coherent brightening in the hottest AIA channels, sensitive to emission from $\log T\,[\mathrm{K}] \gtrsim 6.7$ plasma and the presence of particle acceleration as obtained from hydrodynamic modeling (Testa et al. 2014; Polito et al. 2018). Ugarte-Urra & Warren (2014) and Ugarte-Urra et al. (2017, 2019) have studied transient loops in active region cores observed in the Fe XVIII emission of the AIA 94 Å passband and investigated (a) their frequency (Ugarte-Urra & Warren 2014), (b) the relation between total Fe XVIII emission and total unsigned flux of the active region (Ugarte-Urra et al. 2017), and (c) the relation between the Fe XVIII emission in each of these impulsively heated loops and the magnetic (B_{avg}) and geometric (loop length, L) properties of the loop (Ugarte-Urra et al. 2019). Here we focus on the observed morphology of the AIA 94 and 131 Å hot emission in each of these IRIS events, which suggests that the impulsive heating derives from large-scale magnetic rearrangements/large angle reconnection. The interaction of small loops has been taken as explanation of a small flare observed with IRIS (Alissandrakis et al. 2017), and our study provides direct evidence from the morphology observed in the hot AIA channels counterparts. Many recent papers have studied simultaneous observations from IRIS and *SDO*/AIA to investigate magnetic rearrangements causing localized brightenings in the transition region, and likely related with flux emergence (e.g., Jiang et al. 2015; Toriumi et al. 2017; Guglielmino et al. 2018, 2019; Huang 2018; Tian et al. 2018). However, we note that the coronal heating events we study here have quite different properties with respect to those events, in that they have generally lower Doppler shift velocities (up to $\sim\pm 30$ km s^{-1}) and show heating of the overlying coronal loops to several MK.

The evolution and the energetic scale of the events make them intermediate—and are therefore valuable links—between intense flares and diffuse nanoflare activity. They are also at the

right scale to be as intense and coherent as to let us study their evolution in good detail.

The observed complex evolution cannot be described by simple hydrodynamic models and requires detailed MHD modeling. Although self-standing, a natural extension of this work will be the attempt to model this specific kind of large-scale magnetic interaction through detailed MHD simulations, which will be the subject of a forthcoming work. It will also be very important to acquire more complete observational evidence, through large band spectroscopy.

F.R. and A.P. acknowledge support from Italian Ministero dell'Istruzione, dell'Università e della Ricerca. P.T. acknowledges support by NASA grants NNX15AF50G and NNX15AF47G, and by contracts 8100002705 and SP02H1701R from Lockheed-Martin to SAO. The authors thank the International Space Science Institute (ISSI) for their support and hospitality during the meetings of the ISSI team "New Diagnostics of Particle Acceleration in Solar Coronal Nanoflares from Chromospheric Observations and Modeling."

Appendix A
Animations

Animations of the loop evolution shown in Figures 2–6 are available in Figures 9–11 in this appendix. In each case the 94 Å and 131 Å images are in the left- and right-hand panels of the animations, respectively. The real-time duration of the animations correspond to ∼1000 s as traced in the light curves shown in Figures 4–6.

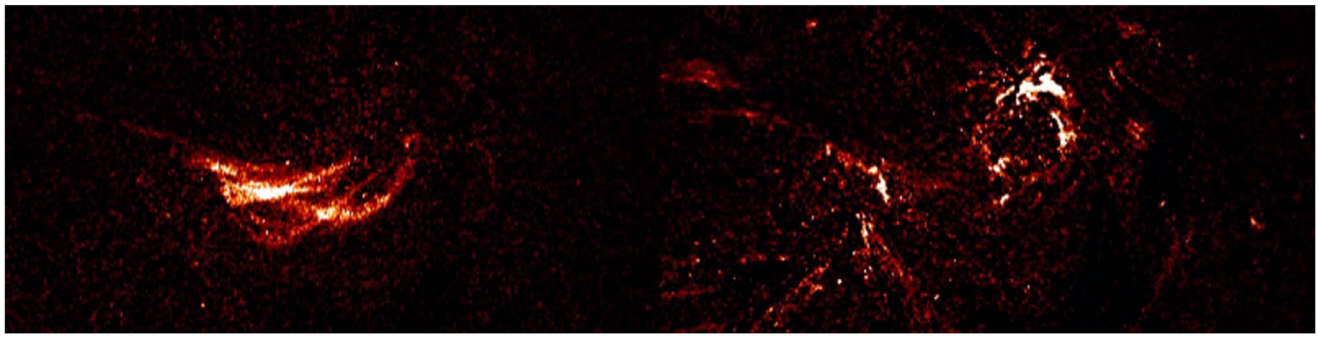

Figure 9. Animation of the 2015 November 12 (Event 9 in Table 1) loop system in the AIA 94 Å (left) and AIA 131 Å (right) channels. The animation corresponds to the static panels shown in Figures 2 and 3. The animation traces the loop for ∼1000 s starting at 01:37:12 UT.

(An animation of this figure is available.)

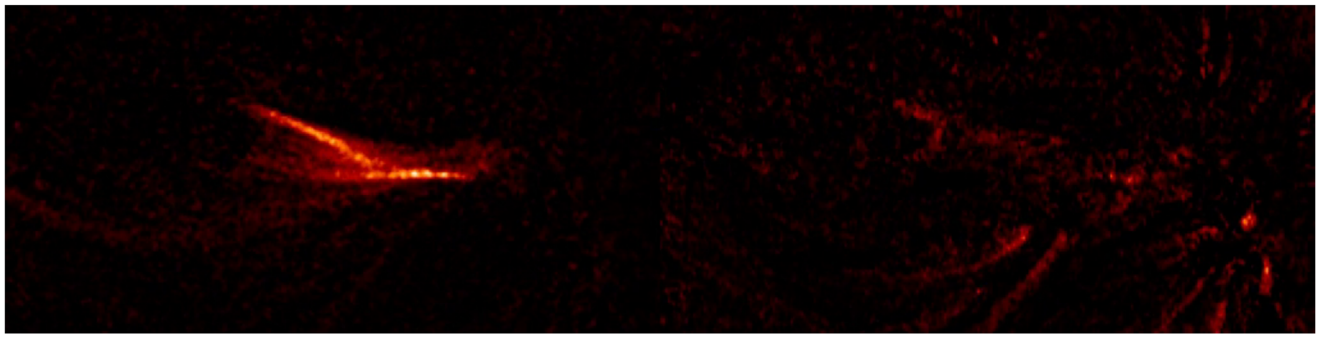

Figure 10. Animation of the 2014 September 18 (Event 7 in Table 1) loop system in the AIA 94 Å (left) and AIA 131 Å (right) channels. The animation corresponds to the static panels in Figure 5. The animation traces the loop for ∼1500 s starting at 08:06:01 UT.

(An animation of this figure is available.)

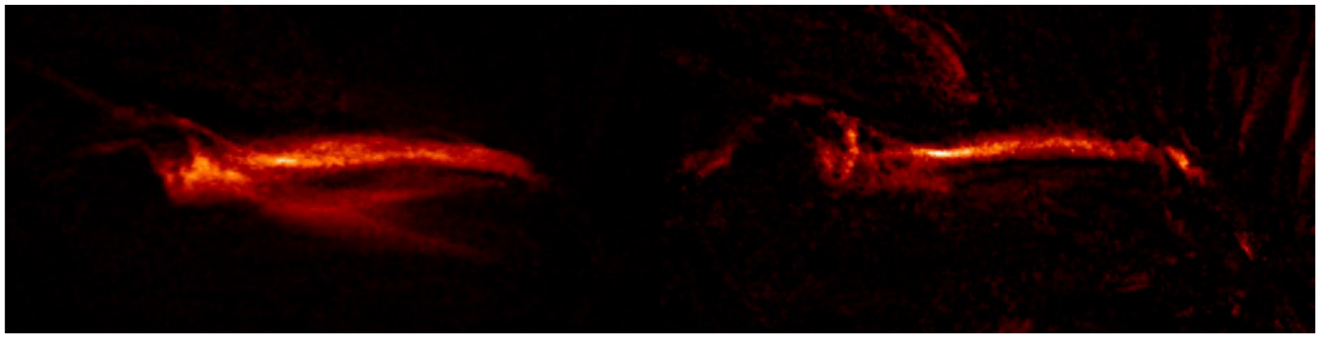

Figure 11. Animation of the 2014 September 17 (Event 5 in Table 1) loop system in the AIA 94 Å (left) and AIA 131 Å (right) channels. The animation corresponds to the static panels shown in Figure 6. The animation traces the loop for ∼1600 s starting at 14:52:01 UT.

(An animation of this figure is available.)

Appendix B
Other Events

Figure 12 shows representative images of the other events listed in Table 1, taken in the 94 Å channel. All of them show complex magnetic configurations.

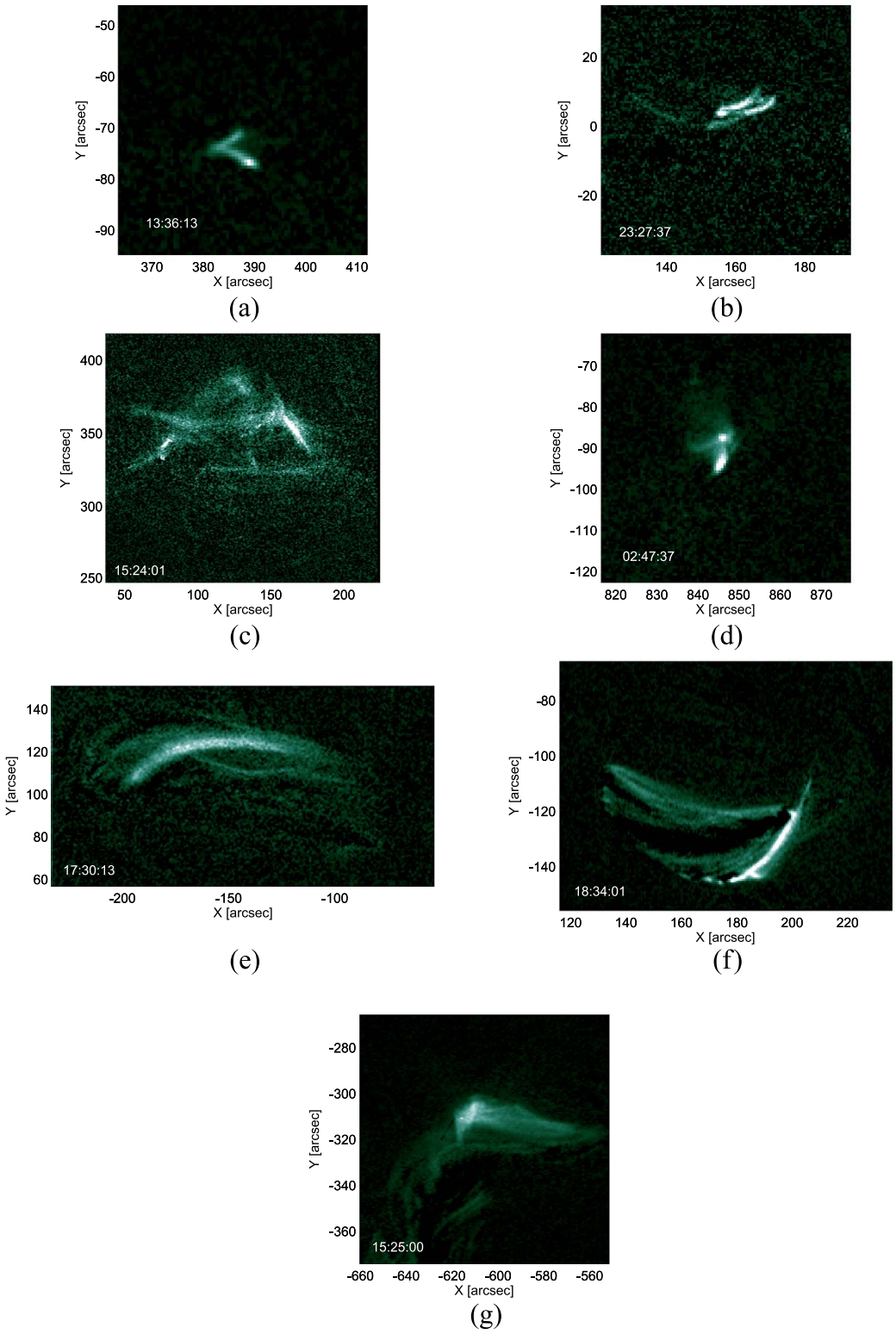

Figure 12. Representative images of the other events (at the labeled times) listed in Table 1 taken in the 94 Å channel: (a) 1 (2014 February 4), (b) 2 (2014 February 23), (c) 3 (2014 March 19), (d) 4 (2014 April 10), (e) 6 (2014 September 17), (f) 8 (2015 January 29), (g) 10 (2015 December 24).

ORCID iDs

Fabio Reale https://orcid.org/0000-0002-1820-4824
Paola Testa https://orcid.org/0000-0002-0405-0668

References

Alissandrakis, C. E., Koukras, A., Patsourakos, S., & Nindos, A. 2017, A&A, 603, A95
Argiroffi, C., Peres, G., Orlando, S., & Reale, F. 2008, A&A, 488, 1069
Aschwanden, M. J., Stern, R. A., & Güdel, M. 2008, ApJ, 672, 659
Boerner, P., Edwards, C., Lemen, J., et al. 2012, SoPh, 275, 41
Boerner, P. F., Testa, P., Warren, H., Weber, M. A., & Schrijver, C. J. 2014, SoPh, 289, 2377
Brosius, J. W., Daw, A. N., & Rabin, D. M. 2014, ApJ, 790, 112
Cargill, P. J., Warren, H. P., & Bradshaw, S. J. 2015, RSPTA, 373, 20140260
Cheung, M. C. M., Boerner, P., Schrijver, C. J., et al. 2015, ApJ, 807, 143
Foster, A. R., & Testa, P. 2011, ApJL, 740, L52
Guglielmino, S. L., Young, P. R., & Zuccarello, F. 2019, ApJ, 871, 82
Guglielmino, S. L., Zuccarello, F., Young, P. R., Murabito, M., & Romano, P. 2018, ApJ, 856, 127
Hannah, I. G., Hudson, H. S., Battaglia, M., et al. 2011, SSRv, 159, 263
Huang, Z. 2018, ApJ, 869, 175
Hudson, H. 1991, SoPh, 133, 357
Ishikawa, S.-n., Glesener, L., Krucker, S., et al. 2017, NatAs, 1, 771
Jeffrey, N. L. S., Fletcher, L., Labrosse, N., & Simões, P. J. A. 2018, SciA, 4, 2794
Jiang, F., Zhang, J., & Yang, S. 2015, PASJ, 67, 78
Klimchuk, J. 2006, SoPh, 234, 41
Ko, Y.-K., Doschek, G., Warren, H., & Young, P. 2009, ApJ, 697, 1956
Lemen, J. R., Title, A. M., Akin, D. J., et al. 2012, SoPh, 275, 17
Lin, A. C., Nightingale, R. W., & Tarbell, T. D. 2001, SoPh, 198, 385
Marsh, A. J., Smith, D. M., Glesener, L., et al. 2018, ApJ, 864, 5
Martínez-Sykora, J., De Pontieu, B., Testa, P., & Hansteen, V. 2011, ApJ, 743, 23
McTiernan, J. 2009, ApJ, 697, 94
Miceli, M., Reale, F., Gburek, S., et al. 2012, A&A, 544, A139
Mitra-Kraev, U., & Del Zanna, G. 2019, A&A, 628, A134
Narukage, N., Sakao, T., Kano, R., et al. 2011, SoPh, 269, 169
Parenti, S., del Zanna, G., Petralia, A., et al. 2017, ApJ, 846, 25
Parker, E. 1988, ApJ, 330, 474
Petralia, A., Reale, F., Testa, P., & Del Zanna, G. 2014, A&A, 564, A3
Polito, V., Testa, P., Allred, J., et al. 2018, ApJ, 856, 178
Porter, L., & Klimchuk, J. 1995, ApJ, 454, 499
Priest, E., & Forbes, T. 2000, Magnetic Reconnection (New York: Cambridge Univ. Press)
Reale, F. 2007, A&A, 471, 271
Reale, F., Guarrasi, M., Testa, P., et al. 2011, ApJL, 736, L16
Reale, F., Testa, P., Klimchuk, J., & Parenti, S. 2009, ApJ, 698, 756
Serio, S., Reale, F., Jakimiec, J., Sylwester, B., & Sylwester, J. 1991, A&A, 241, 197
Testa, P., De Pontieu, B., Allred, J., et al. 2014, Sci, 346, 1255724
Testa, P., Drake, J. J., & Landi, E. 2012, ApJ, 745, 111
Testa, P., & Reale, F. 2012, ApJL, 750, L10
Tian, Z., Shen, Y., & Liu, Y. 2018, NewA, 65, 7
Toriumi, S., Katsukawa, Y., & Cheung, M. C. M. 2017, ApJ, 836, 63
Ugarte-Urra, I., Crump, N. A., Warren, H. P., & Wiegelmann, T. 2019, ApJ, 877, 129
Ugarte-Urra, I., & Warren, H. P. 2014, ApJ, 783, 12
Ugarte-Urra, I., Warren, H. P., Upton, L. A., & Young, P. R. 2017, ApJ, 846, 165